The Astrophysical Journal, 742:131 (11pp), 2011 December 1 doi:10.1088/0004-637X/742/2/131

UNCOVERING THE WAVE NATURE OF THE EIT WAVE FOR THE 2010 JANUARY 17 EVENT THROUGH ITS CORRELATION TO THE BACKGROUND MAGNETOSONIC SPEED

X. H. Zhao[1,2], S. T. Wu[2], A. H. Wang[2], A. Vourlidas[3], X. S. Feng[1], and C. W. Jiang[1]
[1] SIGMA Weather Group, Sate Key Laboratory of Space Weather, Center for Space Science and Applied Research, Chinese Academy of Sciences, Beijing 100190, China; xhzhao@spaceweather.ac.cn
[2] Center for Space Plasma and Aeronomic Research and Department of Mechanical and Aerospace Engineering, University of Alabama in Huntsville, Huntsville, AL 35899, USA; wus@uah.edu
[3] Space Sciences Division, Naval Research Laboratory, Washington, DC 20375, USA
Received 2011 April 20; accepted 2011 September 5; published 2011 November 15

ABSTRACT

An EIT wave, which typically appears as a diffuse brightening that propagates across the solar disk, is one of the major discoveries of the Extreme ultraviolet Imaging Telescope on board the *Solar and Heliospheric Observatory*. However, the physical nature of the so-called EIT wave continues to be debated. In order to understand the relationship between an EIT wave and its associated coronal wave front, we investigate the morphology and kinematics of the coronal mass ejection (CME)–EIT wave event that occurred on 2010 January 17. Using the observations of the SECCHI EUVI, COR1, and COR2 instruments on board the *Solar Terrestrial Relations Observation-B*, we track the shape and movements of the CME fronts along different radial directions to a distance of about 15 solar radii (R_s); for the EIT wave, we determine the propagation of the wave front on the solar surface along different propagating paths. The relation between the EIT wave speed, the CME speed, and the local fast-mode characteristic speed is also investigated. Our results demonstrate that the propagation of the CME front is much faster than that of the EIT wave on the solar surface, and that both the CME front and the EIT wave propagate faster than the fast-mode speed in their local environments. Specifically, we show a significant positive correlation between the EIT wave speed and the local fast-mode wave speed in the propagation paths of the EIT wave. Our findings support that the EIT wave under study is a fast-mode magnetohydrodynamic wave.

Key words: shock waves – Sun: coronal mass ejections (CMEs) – Sun: UV radiation

Online-only material: color figures

1. INTRODUCTION

The so-called EIT waves or EUV waves, discovered by the *Solar and Heliospheric Observatory* (*SOHO*) Extreme ultraviolet Imaging Telescope, are expanding wave-like structures in coronal emission lines (Moses et al. 1997; Thompson et al. 1998, 1999). These coronal EUV enhancements usually have a global-scale circular wave front appearance and can propagate over most of the visible solar surface followed by expanding dimmings. EIT observations demonstrate that they propagate across the solar disk at typical velocities of 200–400 km s^{-1} (Thompson & Myers 2009). Other bands of wavelength, such as X-rays (Narukage et al. 2002; Hudson et al. 2003; Warmuth et al. 2005) and microwaves (White & Thompson 2005; Vršnak et al. 2005), also observed similar waves. EIT waves are generated near an active region (AR), propagating outward into the quiet Sun at an almost constant altitude. Some observations demonstrate that the EIT waves tend to avoid ARs and stop at the boundaries of coronal holes (Thompson et al. 1998, 1999; Wills-Davey & Thompson 1999; Wu et al. 2001) as well as near the separatrix between ARs, where they may appear as a "stationary" front (Delannée & Aulanier 1999). Statistical studies demonstrate that nearly all EIT waves are correlated to coronal mass ejections (CMEs) and weakly correlated to flares, at least for those EIT waves that have a very bright propagating front (Biesecker et al. 2002).

The physical nature of EIT waves has been the subject of strong debate since their discovery. Generally speaking, the models for EIT waves can be divided into four groups: (1) a fast-mode magnetohydrodynamic (MHD) wave model, (2) a soliton or slow-mode MHD wave model, (3) a pseudo-wave model, and (4) a hybrid model. EIT waves have been successfully modeled as fast-mode waves (Thompson et al. 1999; Wills-Davey & Thompson 1999; Wang 2000; Wu et al. 2001, 2005; Ofman & Thompson 2002; Warmuth et al. 2004; Ballai et al. 2005; Patsourakos et al. 2009). This interpretation can successfully explain the refraction and deflection of EIT waves when interacting with ARs and coronal holes, where the Alfvén velocity is higher than that in the quiet Sun (see an example in Gopalswamy et al. 2009). The soliton or slow-mode MHD wave model interprets the EIT wave as a soliton-like wave (Wills-Davey et al. 2007) or as a disturbance in the corona caused by the slow shock and the velocity vortices (Wang et al. 2009). The pseudo-wave model suggests that EIT waves are not real waves but instead are the consequence of the reconfiguration of magnetic field lines during a CME liftoff (Delannée & Aulanier 1999; Delannée 2000). They could also be due to the successive stretching or opening of closed field lines covering the erupting flux rope (Chen et al. 2002, 2005), the generation of currents (Delannée et al. 2007, 2008), or the driven magnetic reconnections between the skirt of the expanding CME magnetic field and the favorably orientated quiet-Sun magnetic field (Attrill et al. 2007a, 2007b). The hybrid model postulates that EIT waves consist of two components, and they are the result of a combination of both wave and non-wave mechanisms (Zhukov & Auchère 2004; Cohen et al. 2009; Liu et al. 2010). Recent detailed three-dimensional (3D) MHD simulations (Downs et al. 2011) are fully consistent with the fast-mode wave interpretation and show that the EIT wave is a fast-mode MHD wave, while the brighter emission behind it is associated with the erupting CME as first suggested by Patsourakos & Vourlidas (2009). The Downs et al. (2011) results contradict the Cohen et al. (2009)

interpretation of their simulation. Details of these models can be seen in recent review papers (Warmuth 2007; Vršnak & Cliver 2008; Wills-Davey & Attrill 2009; Gallagher & Long 2011).

One of the major reasons that hindered our understanding of the nature of the EIT waves was the single-point observation and low cadence of EIT (no better than 12 minutes) during the *SOHO* epoch. The Extreme Ultraviolet Imager (EUVI) instruments on board the *Solar Terrestrial Relations Observatory* (*STEREO*) present a new opportunity to study the coronal activities because of the high cadence in both time and spatial resolution. The large field of view (FOV) of the EUVI (1.7 R_s) and its combination with the white-light coronagraphs of COR1 and COR2 can provide observations to study the structure and kinematics of global EIT waves together with the evolution of their associated CMEs. Until now, many case studies of the EIT wave have been carried out using the data from *STEREO*/EUVI (Long et al. 2008; Veronig et al. 2008; Ma et al. 2009; Kienreich et al. 2009; Patsourakos et al. 2009). On the other hand, there should be a positive correlation between the EIT wave propagation speed and the local fast-mode wave speed in the context of the fast-wave model. However, one would not see a significant positive correlation between the EIT wave speed and the local fast-mode wave speed in the pseudo-wave model. In particular, Yang & Chen (2010) investigated the relation between the EIT wave velocity and the local magnetic field in the corona and found significant negative correlation between them in the propagating trajectories of the wave front. This is the starting point of this paper. We will investigate the morphology and kinematic processes of the 2010 January 17 CME–EIT wave event using the SECCHI EUVI, COR1, and COR2 instruments (Howard et al. 2008) on board the *STEREO* mission (Kaiser et al. 2008), and we will compare their moving speed to the characteristic speeds of the background in order to disclose the physical nature of the EIT wave.

2. EVENT DESCRIPTION

On 2010 January 17, the *STEREO-B* observed a clear EIT wave event associated with a CME eruption. This event erupted from AR National Oceanic and Atmospheric Administration 11041 at the location of S25E128 as viewed from Earth. The EUV transient was first observed at 03:47 UT and fully observed at four wave bands of EUVI (171 Å, 195 Å, 284 Å, and 304 Å). The *STEREO-B* was located 69.°2 behind Earth on its orbit around the Sun during this time, and it was the only spacecraft to observe the EUV transient among the *SOHO* and the *STEREO*. The Hiraiso Radio Spectrograph (HIRAS) recorded a high-frequency type II radio burst drifting from ∼310 MHz to ∼80 MHz during ∼03:51–03:58 UT (http://sunbase.nict.go.jp/solar/denpa/spe_summary/2010/spe201001.txt). The *SOHO*/C2 began to observe the corresponding CME at 04:50 UT. It was a partial halo CME in the Large Angle Spectrometric Coronograph's (LASCO) FOV with a projected angular width of 126°. The CME propagated in the southeast quadrant in the plane of sky of LASCO along a central position angle of 114° (relative to the solar north). This is a backside CME in the view of *SOHO*, and its propagation direction is consistent with the source location of the AR. The average speed and deceleration of this CME in LASCO's FOV are 350 km s^{-1} and −4.1 m s^{-2}, respectively (with an error of 10%). More information about LASCO's observations of the CME can be found in the Coordinated Data Analysis Workshops Data Center's CME catalog (http://cdaw.gsfc.nasa.gov/CME_list/UNIVERSAL/2010_01/univ2010_01.html). The advantage of studying this particular event is that the EIT wave front and the CME front are clearly observed simultaneously by the EUVI on board *STEREO-B*. Thus, it is convenient for us to study the propagating process of the EIT wave and the CME front synchronously and probe the relationship between them. Veronig et al. (2010) have studied this event. They found that the observed coronal bright structure in EUV observation was the wave dome (called a "dome-shaped coronal wave"). This is the clearest observation of a dome-shaped wave so far. The coronal bright structure was formed by a weak shock wave and the upward moving part of the shock wave was driven all the time (Veronig et al. 2010). However, the properties of this event found from EUV, white light, and a metric type II burst match expectations for a freely expanding coronal shock wave, including correspondence to the fast-mode speed distribution, while the transient sweeping over the solar surface had a speed typical of EIT waves (Grechnev et al. 2011).

3. KINEMATIC TRACKING

We use the observations of EUVI-B (FOV: up to 1.7 R_s) 195 Å to track the movement of the EIT wave front along 10 fixed paths of large circles on a spherical surface, as shown in the left panel of Figure 1. The blue solid lines passing through the source location (S) denote these paths of large circles, where each path is separated by 20° and labeled with the number "1," "2," "3,"..., "10" for discrimination. Here, the source location stands for the location of AR 11041, which is believed to be the erupting source of this CME/EIT wave event. The imaging cadence of EUVI 195 Å is 5 minutes. As for the CME front, we use the combination of the observations of EUVI-B 195 Å, COR1-B (FOV: 1.5–4 R_s), and COR2-B (FOV: 2.5–15 R_s) to track its movement outward along fixed radial directions relative to the source location, shown in both panels of Figure 1. The red dotted lines denote the radial directions to track the CME front. Each direction is drawn at fixed position angles (P.A.s) relative to the source location. The tracking method used here is the same as that used by Zhao et al. (2010). It is a semi-automatic method, meaning that the display of images and plotting of the P.A. lines or tracking paths are drawn automatically by interactive data language procedures. Identifying the fronts needs human intervention. However, each tracking can be repeated several times in order to reduce the subjective uncertainties. Of note, our tracking of the CME front is made relative to the source location, which is different from the traditional way, i.e., relative to the Sun center.

4. KINEMATIC ANALYSIS

Figure 2 shows our tracking results for the evolution of the EIT wave (left panel) and the CME front (right panel). The EIT wave is propagating outward from the source location as a circular bright front, which is a typical characteristic of an EIT wave in the EUV observations. Specifically, the wave front is clearer in the northern area of paths "1," "2,"..., "5" than in the southern area of paths "6," "7,"..., "10" as indicated in Figure 1, so the southern parts of the wave cannot be traced as far as the northern parts. The leading edge of the CME is a CME front with a bubble-like shape and outward movement relative to the original source. The CME fronts observed by EUVI are denoted by solid lines, while those observed by COR1 are denoted by dashed lines. It should be noted that the EUVI CME fronts are co-spatial with the COR1 CME

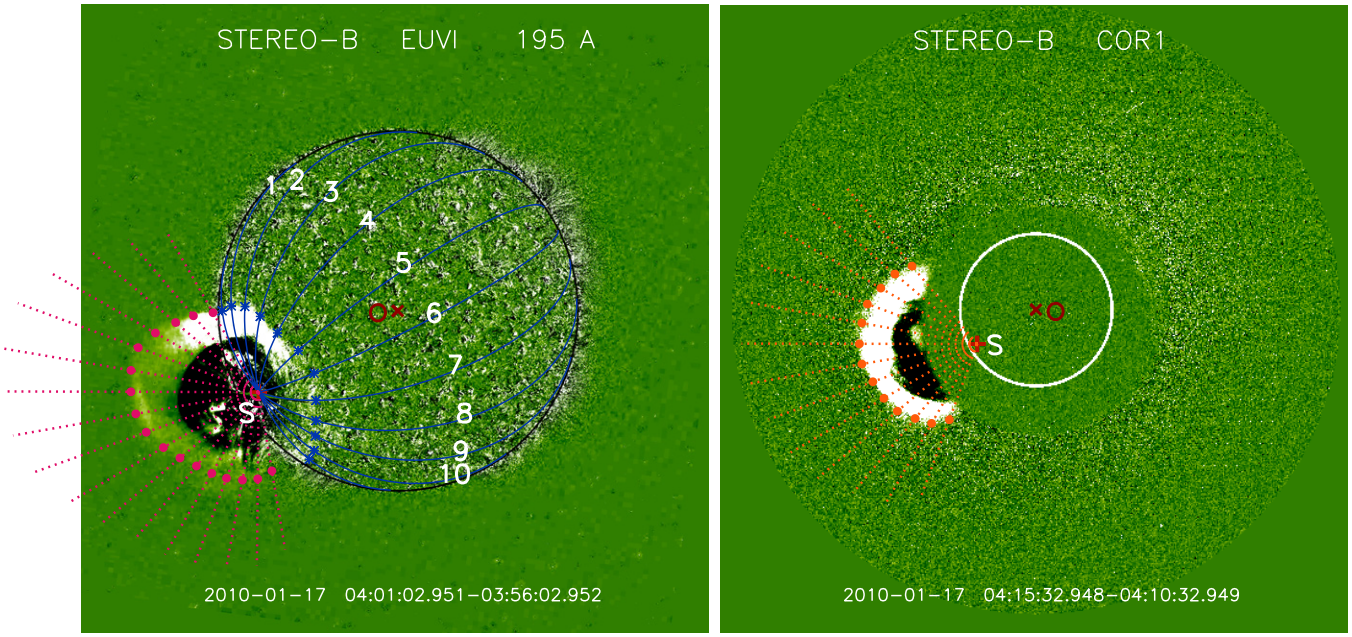

Figure 1. Example of tracking the fronts of the EIT wave and its associated CME front. O is the Sun center; S is the source location of the event. The red dotted lines passing through the source location denote the radial directions with fixed P.A.s to track the CME front. The P.A. is measured counterclockwise from the solar north. The blue large circles in the left panel denote the propagation paths of the EIT wave on the solar surface, where numbers "1," "2," "3,"..., "10" denote those tracking paths used in Figures 5 and 6. The white circle in the right panel represents the solar disk.

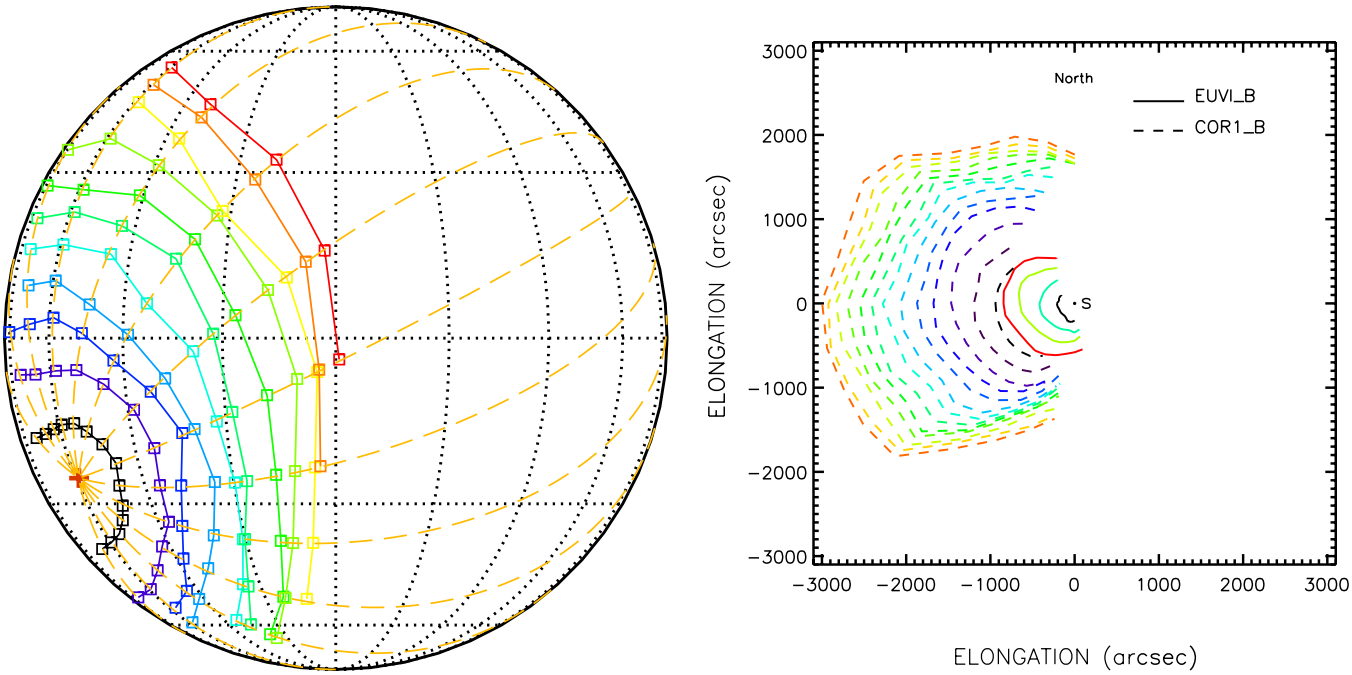

Figure 2. Evolution of the EIT wave on the solar surface (left panel) and the evolution of the CME front (right panel). The CME fronts observed by EUVI are denoted by the solid lines and those observed by the COR1 are denoted by the dashed lines.

fronts at the same time, linking up very well in both time and space. Chen (2009) recognized the low-coronal fronts above the limb in the EIT 195 Å image as "EIT wave" fronts and found that they were co-spatial with the CME leading loops in white light for the 1997 September 9 event. He suggested that the "EIT waves are the EUV counterparts of the CME leading loop." However, Patsourakos & Vourlidas (2009) used quadrature EUVI and COR1 observations with high cadence to clearly show that the EUVI wave is associated with the shock front ahead of the expanding CME loops, which was expected by the wave interpretation. Veronig et al. (2010) reached the same conclusion for our event and recognized the low-coronal EUV fronts above the limb as the wave dome (not the CME). In fact, they concluded that the dome was formed by a weak shock wave. Grechnev et al. (2011) pointed out that the dome was a plasma flow successively involved into the motion by the freely propagating shock front, i.e., the leading part of the transient was a CME by definition, but it was a shock-driven plasma flow. Here we call the EUV fronts above the limb the "CME front" in order to distinguish it from the EIT wave front on the solar disk.

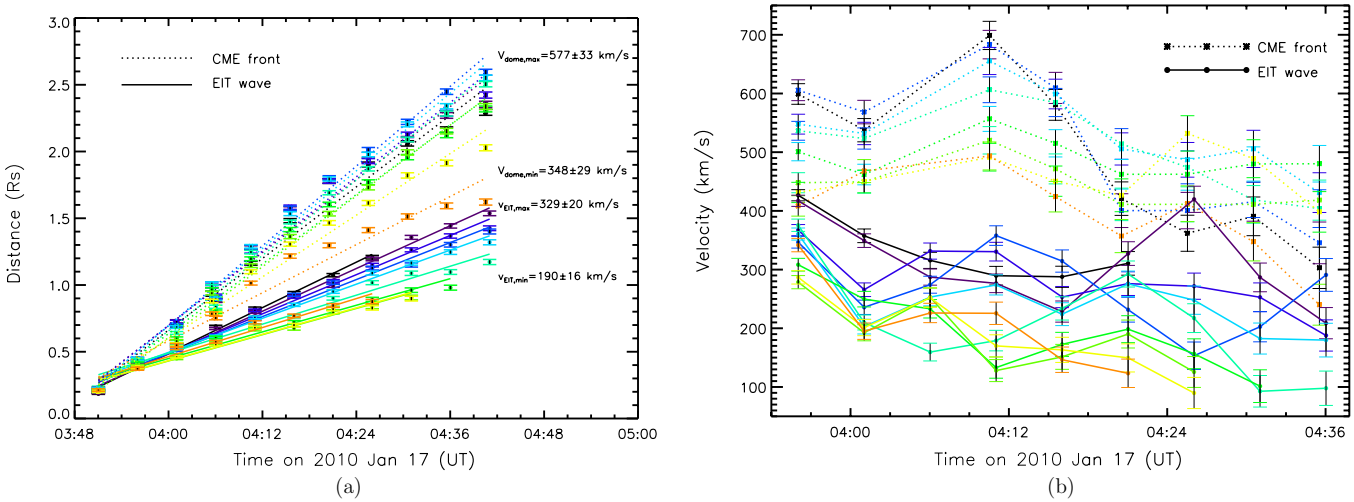

Figure 3. Distance–time plots (left panel) and velocity–time plots (right panel) for the CME front and the EIT wave front. Different lines denote the results from different paths (for the EIT wave) or different radial directions (for the CME front). The error bar on each point is also shown.

(A color version of this figure is available in the online journal.)

We will demonstrate that this front, although called a "CME front," is really associated with the shock front in the most outer part of the CME. So the "CME front" in this paper consists of both the "EUVI CME front" (in EUVI) and the "white-light CME front" (in COR1 and COR2).

Figure 3 shows the tracking results for the kinematics of the EIT wave as well as the CME front. Here we use only the observations of EUVI and COR1 for the CME in order to simultaneously compare the kinematics of the EIT wave and the CME front. The left panel gives the distance versus time for the EIT wave and the CME front. The distance of the EIT wave is computed from the source region on a spherical surface with a height of 72 Mm above the photosphere. The height of 72 Mm is fully consistent with the coronal scale height of the quiet Sun (∼70 Mm at 1.5 MK) and is expected since the wave propagates over the quiet Sun, which was as first discovered by Patsourakos et al. (2009). Stereoscopic analysis by Patsourakos et al. (2009) found a wave height of 90 Mm for another event, and Kienreich et al. (2009) reached a similar estimate (80–100 Mm). For the CME front, the distance is measured against the plane of the sky from the source location as the starting point. Different lines denote the tracking results along different paths (for the EIT wave) or different radial directions (for the CME front). The first-order fit to the distance–time plot gives the average velocity of the EIT wave and the CME front within the tracking distance. In the main propagation direction, the CME velocity is 577 ± 33 km s^{-1} and the EIT wave velocity is 329 ± 20 km s^{-1}. Here, the main propagation direction refers to the fastest propagation direction of the EIT wave and the CME front, which is path "1" for the EIT wave and the radial direction of P.A. = 90° for the CME front. The upward propagation velocity of the CME front is nearly twice the lateral propagation velocity of the EIT wave on the solar surface. For other directions/paths, the velocities of the EIT wave and the CME front are smaller because of the projection effect. These results are consistent with Veronig et al. (2010). The right panel gives the velocity variation for the EIT wave and the CME front, which are computed from the adjacent distance measurements using a numerical differentiation with three-point Lagrangian interpolation. The CME front undergoes a clear deceleration process, which is verified by the negative acceleration (−4.1 m s^{-2}) in LASCO's FOV. A predominantly constant speed propagation with a slight deceleration can be seen for the EIT wave. This slight deceleration may be related to the decreasing of the background magnetic field as the wave moves away from the AR. This point will be discussed in Section 6.

5. CORONA BACKGROUND

We use the potential field source surface (PFSS) technique (Schrijver & Derosa 2003) to derive the background magnetic field in the corona as given by Yang & Chen (2010). The input to the PFSS is the synoptic magnetogram of the Michelson Doppler Imager (MDI) telescope on board *SOHO*. The output of the PFSS gives the magnetic field at any point in 3D space between the photosphere and the source surface (chosen to be 2.5 R_s). Figure 4 displays the background coronal magnetic field for this event. The left panel is the distribution of the radial component of magnetic field (B_r) at the photosphere, and the right panel is the 3D coronal magnetic field topology obtained from the PFSS. These images have been rotated to the view direction of *STEREO-B*. It can be seen that the large-scale solar magnetic field is dipole-like, and the AR 11041 is the only recorded large visible active region on the solar disk, which is located at the southeast quadrant. We adopt two heights of the EIT wave above the solar surface for comparison. One is 72 Mm ($R_{\rm wave}$ = 1.104 R_s) as suggested by Patsourakos et al. (2009) and Cohen et al. (2009), while the other is 46 Mm ($R_{\rm wave}$ = 1.067 R_s) as adopted in Yang & Chen (2010). In the computational domain within the source surface ($\leqslant$2.5 R_s), the local magnetic field at each point of the EIT wave front in our tracking paths is calculated by averaging the surrounding points (3 × 3 grids of PFSS) in the extrapolated coronal field at a fixed height of the EIT wave. For the region outside of the source surface, the magnetic field profile is obtained based on magnetic flux conservation ($r^2 B(r)$ = const):

$$B(r) = B(R_{\rm ss}) \times \left(\frac{r}{R_{\rm ss}}\right)^2. \quad (1)$$

Here, $R_{\rm ss} = 2.5 R_s$ is the radius of the source surface and $B(R_{\rm ss})$ is the magnetic field at the source surface.

In order to obtain the fast and slow characteristic speeds in the corona, we also need the density and pressure (or temperature) parameters along the propagating path of the EIT wave and

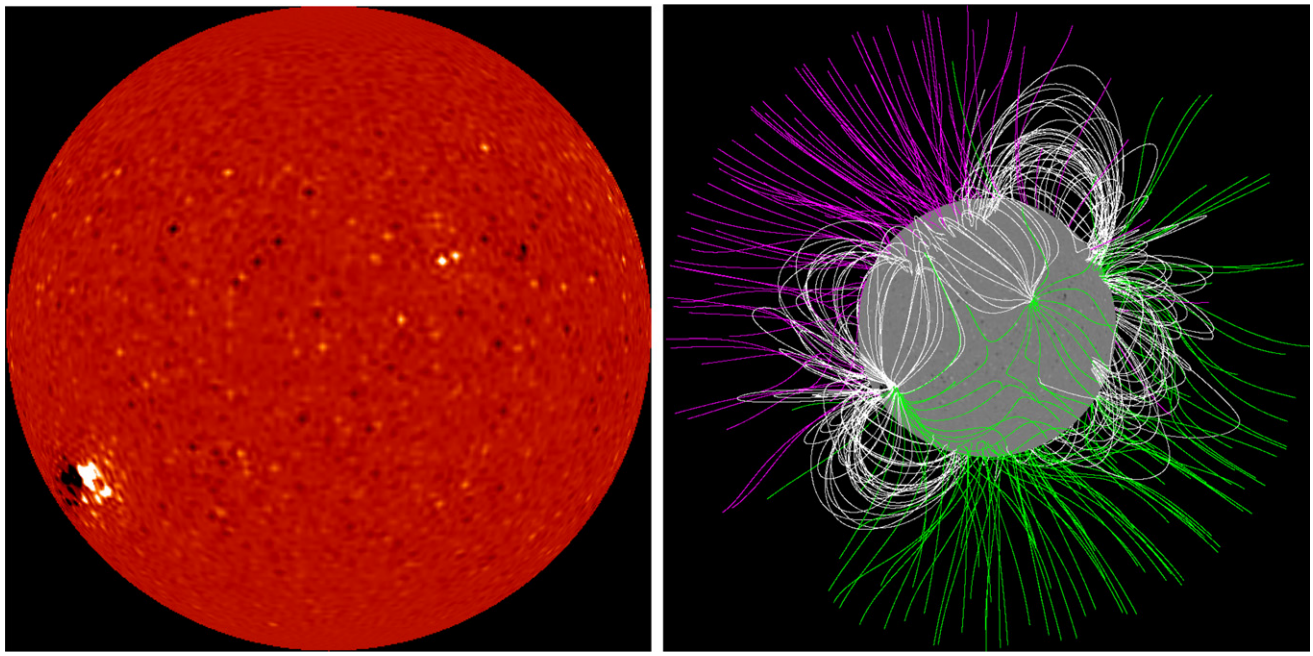

Figure 4. Observed distributions of the radial component of magnetic field (B_r) at the photosphere (left panel) and coronal magnetic field topologies obtained from the PFSS model in the solarsoft distribution (right panel) for this event. The input for the PFSS extrapolation is the synoptic magnetogram of *SOHO*/MDI. The white lines indicate a closed field, and the green and magenta lines are open to heliosphere, with color indicative of polarity. The images in this figure have been rotated to the view direction of *STEREO-B*.

the CME front. However, there is no direct measurement for these parameters. Therefore, we adopt empirical models. For density, we use the Saito density model (Saito et al. 1977) with a multiplicative factor of 10 for the AR corona and a factor of 3 for the quiet corona. That is,

$$n_{\rm AR}(r) = 10 \times (0.0136r^{-2.14} + 1.68r^{-6.13}) \times 10^7 \quad (2)$$

$$n_{\rm QR}(r) = 3 \times (0.0136r^{-2.14} + 1.68r^{-6.13}) \times 10^7, \quad (3)$$

where $n_{\rm AR}$ and $n_{\rm QR}$ (in unit of cm^{-3}) denote the number density in the active region and quiet region, respectively. This method, adopted from Gopalswamy et al. (2001), gives a density of 3×10^9 cm^{-3} at the base of the AR corona and 5×10^8 cm^{-3} at the corona base near the equator as obtained by Fludra et al. (1999). For the pressure above the AR, we use the pressure model given by Gary (2001):

$$p(H) = p_c e^{-(H/H_c)(R/R_s)} + p_k e^{-(H/H_k)(R/R_s)}, \quad (4)$$

where $R = R_s + H$, $H_c = H_0(R/R_s)^2$, $p_c = 1.5$ dyn cm^{-2}, $p_k = 1 \times 10^5$ dyn cm^{-2}, $H_0 = 55$ Mm, $H_k = 0.12$ Mm, and H is the height in unit of Mm.

On the basis of MHD, there are two characteristic propagation speeds: the fast-mode speed (V_f) and the slow-mode speed (V_s), which are given by

$$V_{f,s}^2 = 0.5[(V_A^2 + C_s^2) \pm \sqrt{(V_A^2 + C_s^2)^2 - 4V_A^2 C_s^2 \cos^2\theta}]. \quad (5)$$

Here, θ is the angle between the wave propagation direction and the magnetic field, and V_A and C_s denote the Alfvén speed and sound speed, respectively:

$$V_A = \frac{B}{\sqrt{\mu_0 \rho}}, \quad C_s = \sqrt{\frac{\gamma p}{\rho}}. \quad (6)$$

Theoretically, the polytropic index γ for the solar plasma should lie in the range $1 \leqslant \gamma \leqslant 5/3$. Steinolfson & Hundhausen (1988) demonstrated that $\gamma = 1.05$ gives a reasonable solar wind solution in the corona. Totten et al. (1995) found that the average value of γ for a solar wind proton plasma is 1.46 based on *Helios 1* data. Here we adopt the empirical formula of γ with respect to the radial distance, which is used in Wu et al. (1999):

$$\gamma = \begin{cases} 1.05 & 1 \leqslant r/R_s < 5 \\ 1.05 + \dfrac{1.46 - 1.05}{90}\left(\dfrac{r}{R_s} - 5\right) & 5 \leqslant r/R_s < 95 \\ 1.46 & 95 \leqslant r/R_s \leqslant 220. \end{cases} \quad (7)$$

This formula gives an initial solar wind solution that is close to the observed values at 1 R_s and 1 AU. We compute the sound speed (C_s) of the corona background from 1 R_s to 15 R_s. Here, $\gamma(1R_s) = 1.05$, $\gamma(15R_s) = 1.0955$. So, the contributing effects of γ are only of a factor of 1.0212 ($\sqrt{1.0955}/\sqrt{1.05} = 1.0212$) in our computing domain.

In the case of the propagation perpendicular to the magnetic field ($\theta = 90^\circ$), the fast-mode speed is

$$V_{f\perp} = \sqrt{V_A^2 + C_s^2}. \quad (8)$$

For the propagation parallel to the magnetic field ($\theta = 0$) is

$$V_{f\parallel} = V_A. \quad (9)$$

Because the angle θ is not easy to measure in a real case, here we only consider the extreme cases of perpendicular and parallel propagation of the EIT wave and the CME front. In the case of the EIT wave, we compute the Alfvén speed and sound speed in its propagation path based on Equation (6), where B is from PFSS, $p = 2nkT$, n is from Equation (3), and $T_{\rm wave} = 1.5 \times 10^6$ K corresponding to the observing line of 195 Å. For the CME front, the Alfvén speed and the sound speed in its propagation direction are derived from Equation (6),

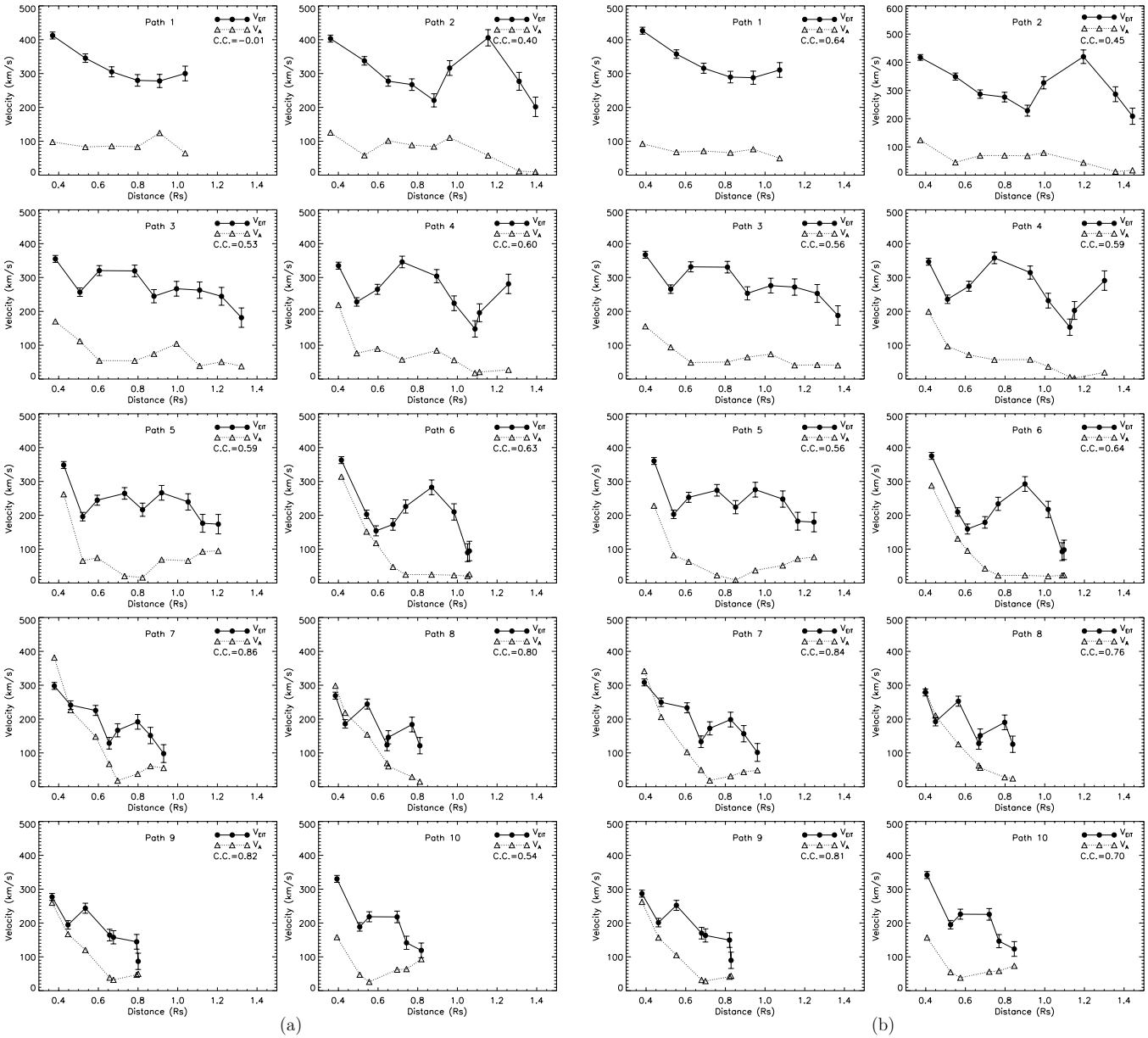

Figure 5. Distribution of the EIT wave speed ($V_{\rm EIT}$) and the corresponding Alfvén wave speed (V_A) plotted vs. the distance of the wave front from the source location. (a) $H_{\rm wave} = 46$ Mm; (b) $H_{\rm wave} = 72$ Mm. The error bar on each point is also shown.

with B from Equation (1) of PFSS, p from Equation (4), and $H_{\rm wave} = 46$ Mm and 72 Mm for comparison. Then $V_{f\perp}$ and $V_{f\parallel}$ are computed according to Equations (8) and (9) in the local environments of the EIT wave and the CME front.

6. TEST OF THE FAST-MODE MHD WAVE MODEL

Figure 5 gives the variation of the plotted EIT wave speed ($V_{\rm EIT}$) and Alfvén speed (V_A) versus the distance of the wave front in the tracking paths. The distance is calculated from the wave front to the source location of the AR 11041 on an assumed spherical surface above the solar disk with the height $H_{\rm wave}$ = (a) 46 Mm and (b) 72 Mm. We can see that both $V_{\rm EIT}$ and V_A drop steadily as the wave propagates farther away from the source location due to the decreasing strength of the magnetic field. The EIT wave clearly propagates faster than the background Alfvén wave in all 10 paths that we tracked. Specifically, these two speeds show significant positive correlation in all the paths for $H_{\rm wave} = 72$ Mm, while only path 1 shows a negative correlation between them for $H_{\rm wave} = 46$ Mm. The correlation coefficient (C.C.) mainly lies in the range of 0.5–0.9. The mean C.C. for $H_{\rm wave} = 72$ Mm is 0.66 with a standard deviation of 0.12, while the mean C.C. for $H_{\rm wave} = 46$ Mm is 0.58 with a standard deviation of 0.24. Therefore, $H_{\rm wave} = 72$ Mm gives a slightly higher C.C. than $H_{\rm wave} = 46$ Mm. These results are different from those obtained by Yang & Chen (2010), which will be addressed in Section 7. Another interesting finding is that the wave propagates faster in the five northern paths, "1," "2,"... , "5," than in the five southern paths, "6," "7,"... , "10." Two reasons are responsible for this phenomenon: first, the wave front is more diffusive in the southern paths so that it is more difficult to determine its front location in these areas (see the left panel of Figure 1); second, the background for the EIT wave in the southern paths is dominated by the open-field regions as well as a southern coronal hole, while the background in the northern paths is dominated by the

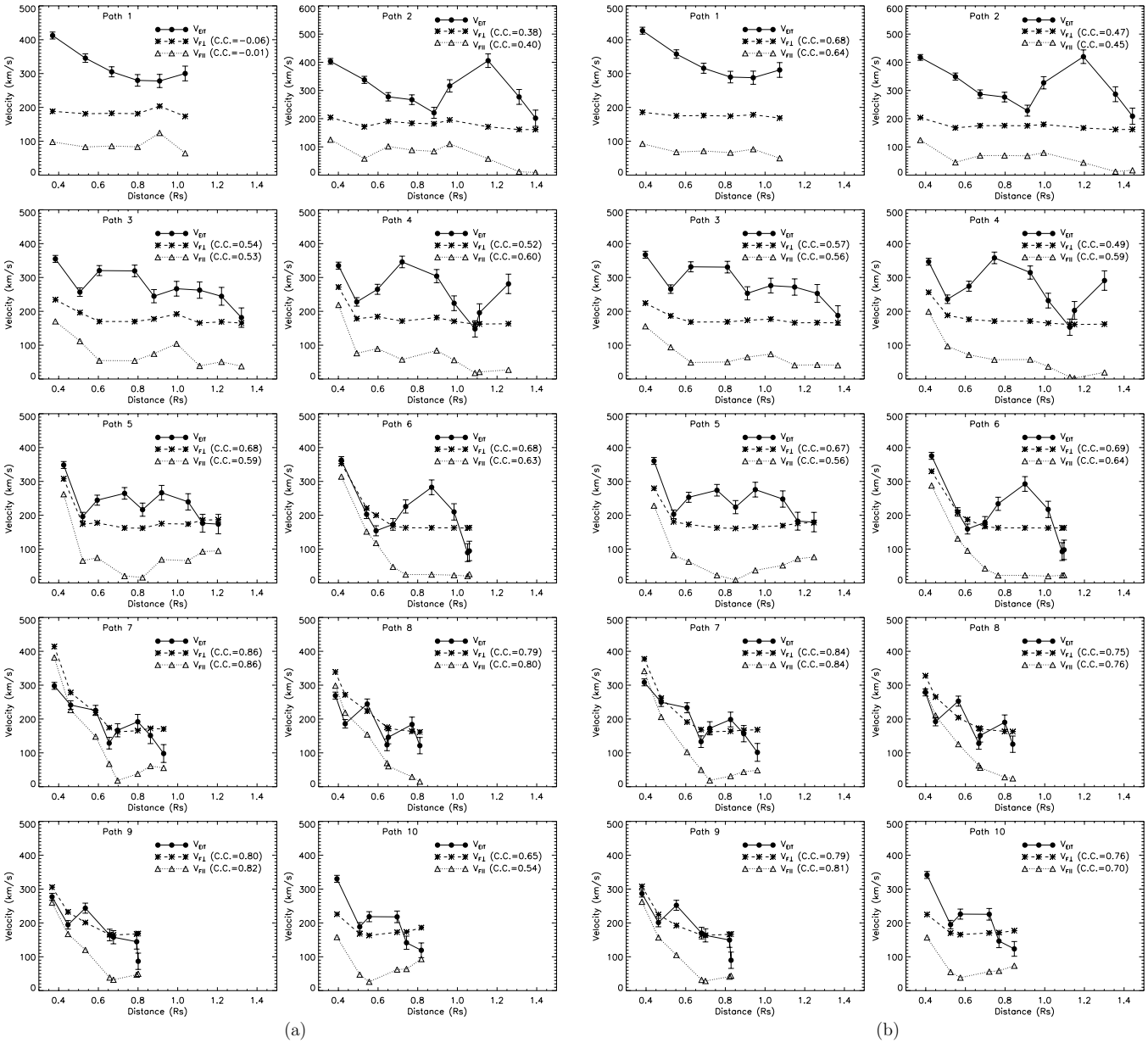

Figure 6. Comparison of $V_{\rm EIT}$, $V_{f\perp}$, and $V_{f\parallel}$, plotted vs. the distance of the wave front from the source location. (a) $H_{\rm wave} = 46$ Mm; (b) $H_{\rm wave} = 72$ Mm. The error bar on each point is also shown.

close-field regions (see the right panel of Figure 4). EIT waves usually appear as "stationary" fronts when they propagate to the boundary of these open-field regions (Thompson et al. 1998, 1999; Wills-Davey & Thompson 1999; Delannée & Aulanier 1999; Wu et al. 2001). Wu et al. (2001) have specifically pointed out that the EIT wave stopped at the coronal hole boundary.

We compute the fast-mode wave speed for the propagation parallel and perpendicular to the magnetic field, $V_{f\perp}$, $V_{f\parallel}$, in the propagation paths of the EIT wave. Figure 6 displays the comparison between $V_{\rm EIT}$ and $V_{f\perp}$, $V_{f\parallel}$ along the tracking paths. The C.C. between $V_{\rm EIT}$ and $V_{f\perp}$, $V_{\rm EIT}$ and $V_{f\parallel}$ are also shown. Figure 6(a) gives the result for $H_{\rm wave} = 46$ Mm and Figure 6(b) gives the result for $H_{\rm wave} = 72$ Mm. In the propagating paths "1," "2,"..., "5," the EIT wave speed ($V_{\rm EIT}$) is evidently faster than both $V_{f\perp}$ and $V_{f\parallel}$, while $V_{\rm EIT}$ is also clearly faster than $V_{f\parallel}$ and at least as fast as $V_{f\perp}$ in the paths "6," "7,"..., "10," except for some isolated points in the trajectory. Specifically, they show positive C.C. between $V_{\rm EIT}$ and $V_{f\perp}$, $V_{\rm EIT}$ and $V_{f\parallel}$. Considering the fact that $V_{f\parallel}$ and $V_{f\perp}$ are two extreme cases and the real fast-mode wave speed should lie between them, we can confidently conclude that the EIT wave is propagating faster than the fast-mode wave within the error range of measurement.

For the CME front, Figure 7 gives its speed profile along the radial distance from the Sun's center. Here, the CME speed ($V_{\rm CME}$) refers to the speed of the CME front in the main propagation direction. The profiles of Alfvén speed (V_A), sound speed (C_S), and solar wind speed ($V_{\rm SW}$) along the radial distance are also given for comparison. The solar wind speed profile that we used is an analytical solution derived by Sheeley et al. (1997) based on the observation of *SOHO*/LASCO between 2 and 30 R_s:

$$V_{\rm SW} = V_a\sqrt{[1 - e^{-(r-r_1)/r_a}]}, \qquad (10)$$

where $V_a = 300$ km s^{-1}, $r_1 = 4.5\ R_s$, and $r_a = 15.2\ R_s$. The Alfvén speed V_A and sound speed C_s are very high above the AR due to the strong magnetic field and high temperature of

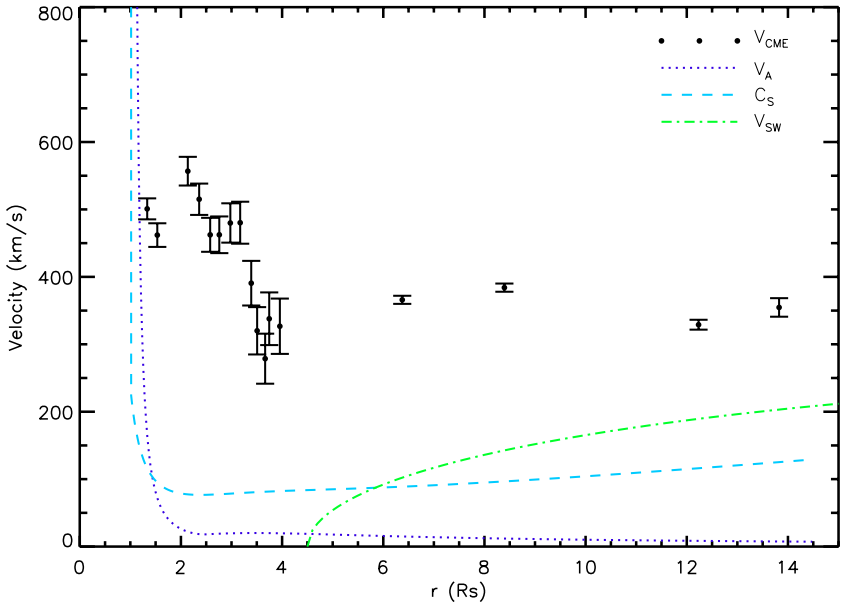

Figure 7. Comparison of the CME speed ($V_{\rm CME}$), the Alfvén speed (V_A), the sound speed (C_s), and the solar wind speed ($V_{\rm SW}$) plotted against the radial distances from the Sun's center. The error bar on each point is also shown.

(A color version of this figure is available in the online journal.)

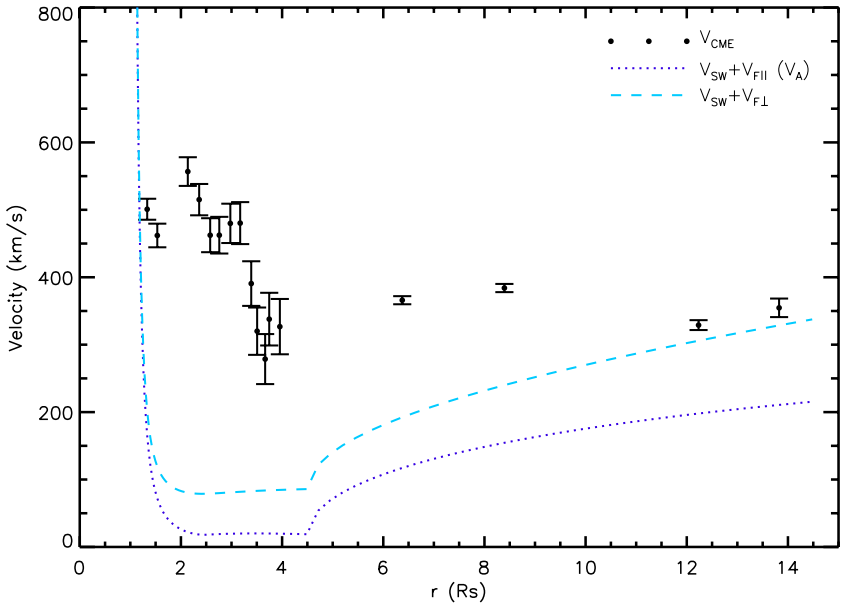

Figure 8. Comparison of $V_{\rm CME}$, $V_{f\perp} + V_{\rm sw}$, and $V_{f\parallel} + V_{\rm sw}$, along the radial distances from the Sun's center. The error bar on each point is also shown.

(A color version of this figure is available in the online journal.)

the plasma. But they drop very quickly with increased radial distance. The radial propagation speed of the CME front is evidently faster than both Alfvén and sound speeds. In order to validate the shock nature of the CME front, we should compare the fast-mode wave speed with the relative speed of the CME front to the solar wind ($V_{\rm CME} - V_{\rm SW}$). Figure 8 gives the variation of $V_{\rm CME}$, $V_{f\perp} + V_{\rm SW}$, and $V_{f\parallel} + V_{\rm SW}$ along the radial distance. It can be seen that this CME undergoes a clear deceleration process within our tracking distance, which is consistent with the observation of *SOHO*/LASCO. But, up to the distance of 14 R_s, its propagation speed relative to the solar wind is evidently higher than the fast-mode wave speed. Therefore, this CME front observed in the white-light coronagraph is the density enhancement from a fast-mode MHD shock. Vourlidas et al. (2003) pointed out that shocks could be directly observed in white-light coronagraph images under suitable conditions, and Ontiveros & Vourlidas (2009) gave several examples of a direct detection of a CME-associated shock in LASCO white-light images.

7. DISCUSSION

We find evidence of a positive correlation between the EIT wave speed $V_{\rm EIT}$ and the local Alfvén speed V_A in its propagating trajectories for this event. However, Yang & Chen (2010) obtained significant negative correlation between the EIT wave speed and the local magnetic field in the corona for their studied events. The difference in these results may come from the different methods of analysis. We and Yang & Chen (2010)

Table 1
Comparison of the C.C. between V_{EIT} and B_r, V_{EIT} and $|B|$

Path	$H_{wave} = 46$ Mm		$H_{wave} = 72$ Mm	
No.	C.C.: V_{EIT} and B_r	C.C.: V_{EIT} and $\|B\|$	C.C.: V_{EIT} and B_r	C.C.: V_{EIT} and $\|B\|$
1	0.49	−0.01	0.44	0.64
2	0.02	0.40	0.15	0.45
3	0.54	0.53	0.66	0.56
4	−0.48	0.60	−0.03	0.59
5	0.30	0.59	0.74	0.56
6	0.46	0.63	0.63	0.64
7	0.18	0.86	0.60	0.84
8	0.69	0.80	0.71	0.76
9	0.56	0.82	0.68	0.81
10	−0.67	0.54	−0.37	0.70
Mean	0.21	0.58	0.42	0.66
σ	0.44	0.24	0.36	0.12

Note. The mean value of the C.C. along these 10 paths as well as its standard deviation (σ) is also given.

used the PFSS model to derive the coronal magnetic field. But, Yang & Chen (2010) investigated the correlation between the EIT wave speed (V_{EIT}) and only the radial component of the magnetic field (B_r), while we computed the Alfvén speed V_A based on the total magnetic field ($|B|$). On the other hand, Yang & Chen (2010) selected 46 Mm as the EIT wave propagating height, and we selected both 46 Mm and 72 Mm as the height of EIT wave to demonstrate the influence of the height. Table 1 shows our results for the C.C. between V_{EIT} and B_r, V_{EIT} and $|B|$ of this event for both $H_{wave} = 46$ Mm and $H_{wave} = 72$ Mm. The mean value of the C.C. along these 10 paths and its standard deviation are also shown in Table 1. The following conclusions can be made from this table: first, the C.C. between V_{EIT} and B_r is lower than that between V_{EIT} and $|B|$ for the same H_{wave}, which demonstrates that the influences of B_θ and B_ϕ cannot be neglected for this range of height in the lower corona; and second, the C.C. are higher in the case of $H_{wave} = 72$ Mm than those in the case of $H_{wave} = 46$ Mm. The correlation between V_{EIT} and B_r for $H_{wave} = 46$ Mm yields the lowest C.C. in our results: in paths "4" and "10," the two parameters show a negative correlation (C.C. of −0.48 and −0.67), and, in paths "2," "5," and "7," only a weak positive correlation can be found (C.C. of 0.02, 0.30, and 0.18). The mean value of these C.C. is 0.21, but their standard deviation is 0.44. So, there is no evidently positive correlation between V_{EIT} and B_r for $H_{wave} = 46$ Mm. The mean value of the C.C. between V_{EIT} and $|B|$ for $H_{wave} = 46$ Mm is 0.58 with a standard deviation of 0.24, larger than that between V_{EIT} and B_r for the same height (0.21 ± 0.44). As for the case of $H_{wave} = 72$ Mm, the mean value of the C.C. between V_{EIT} and B_r and V_{EIT} and $|B|$ is 0.42 and 0.66, with their standard deviations being 0.36 and 0.12, respectively. Another reason that led to the great difference between our results and that of Yang & Chen's (2010) is that their correlation study was applied to the very early phase of the wave, when the wave was probably still driven and not yet a freely propagating fast-mode wave.

According to Figures 5 and 6, the EIT wave is propagating faster than the fast-mode wave speed $V_{f\perp}$, $V_{f\parallel}$ (V_A). For the fast-mode shock, the Mach number is defined as

$$M_\alpha = \frac{V_n}{V_f}, \tag{11}$$

where V_n is the normal component of the relative shock speed. As the EIT wave is propagating circularly outward from the source location on the horizontal plane of the solar disk, there is no measurable background flow in the moving direction of the EIT wave. Therefore, V_n is just the propagating speed of the EIT wave that we tracked. We select V_f to be $V_{f\perp}$ and $V_{f\parallel}$, then compute the corresponding Mach numbers $M_{\alpha\perp}$ and $M_{\alpha\parallel}$, respectively. Figure 9 gives the variation of the Mach number plotted versus time for both perpendicular and parallel propagation to the magnetic field. Here the height of the EIT wave is taken to be 72 Mm. Considering the fact that $M_{\alpha\perp}$ and $M_{\alpha\parallel}$ are two extreme cases for the real Mach number of this event, we can conclude that the EIT wave is propagating with the Mach number evidently larger than unity (horizontal dash-dotted line). Therefore, this EIT wave should be a fast-mode shock in nature. The type II radio burst observed by HIRAS is a direct evidence for the existence of a coronal shock for this event (Veronig et al. 2010), and the starting and ending times of the type II burst are indicated, respectively, as the vertical dash-dotted line and the dashed line in Figure 9 (03:51 UT, 03:58 UT). It is also worth noting that we obtained $\beta < 1$ in the EIT wave paths near the AR, but we obtained $\beta > 1$ in most of the paths in the quiet-Sun regions. $\beta > 1$ implies that the gas pressure is larger than the magnetic pressure in these regions. Hence, the fast-mode wave is dominated by the sonic wave in this case. The large β in these regions may be due to the high temperature $T_{wave} = 1.5 \times 10^6$ K that we used for calculating the sonic wave speed in the quiet-Sun regions. This temperature, which corresponds to the observing line of 195 Å, may be larger than the background corona temperature at the height of 46 Mm and 72 Mm. A lower temperature of the background would lead to $\beta < 1$ in these quiet-Sun regions and subsequently even higher Mach numbers of the EIT wave.

8. CONCLUSIONS

We have made a detailed study of the propagation process of the EIT wave and its associated CME front for the 2010 January 17 event. We tracked the CME front to the distance of 15 R_s along different radial directions. For the associated EIT wave, we tracked its movement along 10 paths on the solar surface up to a distance where it could no longer be clearly identified. The tracking results demonstrated that the CME front undergoes

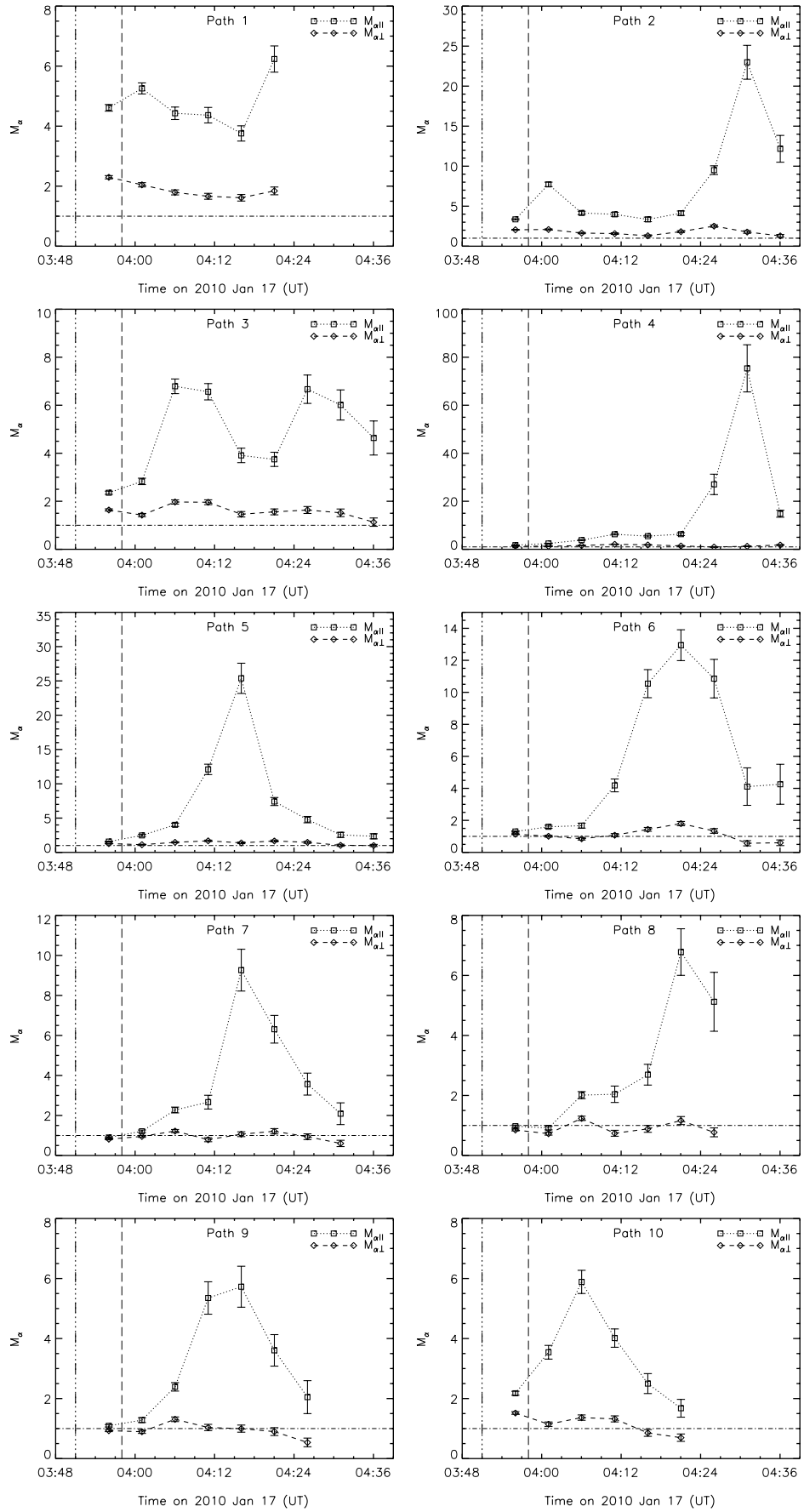

Figure 9. Variation of the Mach number for the EIT wave in the case of perpendicular and parallel propagations to the magnetic field. The horizontal dash-dotted line represents $M_\alpha = 1$, and the vertical dash-dotted line and dashed line denote the starting and ending time of the associated type II burst. The error bar on each point is also shown.

a propagating process of high speed, clear deceleration, while the EIT wave undergoes a propagating process of low speed, slight deceleration. This slight deceleration is caused by the decreasing of the background magnetic field as the wave moves away from the AR. We also investigated the relation between the EIT wave speed, the CME speed, and the local fast-mode characteristic speed. We also found that both the CME front and the EIT wave propagate faster than the fast-mode speed in their local environments. Specifically, a positive correlation exists between the EIT wave speed and the local fast-mode wave speed in the propagation paths of the EIT wave. The Mach number that we computed for this EIT wave is also larger than unity. We conclude that the EIT wave is a fast-mode MHD wave, and in the event under study both the CME front and the EIT wave are a wave phenomenon.

This work is supported by the National Science Foundation under grant ATM 0754378, the Air Force Office of Scientific Research under grant FA9550-07-1-0468, and NASA/Marshall Space Flight Center under cooperative agreement NNM05AA22A. The work is jointly supported by the National Natural Science Foundation of China (41031066, 40921063, 40874091, 40890162, 40904050, 40874077, 41074121, and 41074122), the Specialized Research Fund for State Key Laboratories, and the Knowledge Innovation Program of the Chinese Academy of Sciences. We acknowledge the use of data from *STEREO* and the data from the *SOHO*/*LASCO* CME catalog. The *STEREO*/SECCHI data are produced by a consortium of NRL (US), LMSAL (US), NASA/GSFC (US), RAL (UK), UBHAM (UK), MPS (Germany), CSL (Belgium), IOTA (France), and IAS (France). We thank the *SOHO*/MDI team for the use of their data. *SOHO* is a mission of international collaboration between ESA and NASA. We would also like to thank M. L. Derosa for the help on the use of the PFSS routine and Dr. P. F. Chen for beneficial discussions. Thanks also go to Dr. W. Liu for his assistance in improving this paper. We thank the referee for his/her suggestions.

REFERENCES

Attrill, G. D. R., Harra, L. K., van Driel-Gesztelyi, L., & Démoulin, P. 2007a, ApJ, 656, L101
Attrill, G. D. R., Harra, L. K., van Driel-Gesztelyi, L., Démoulin, P., & Wülser, J.-P. 2007b, Astron. Nachr., 328, 760
Ballai, I., Erdélyi, R., & Pintér, B. 2005, ApJ, 633, L145
Biesecker, D. A., Myers, D. C., Thompson, B. J., Hammer, D. M., & Vourlidas, A. 2002, ApJ, 569, 1009
Chen, P. F. 2009, ApJ, 698, L112
Chen, P. F., Fang, C., & Shibata, K. 2005, ApJ, 622, 1202
Chen, P. F., Wu, S. T., Shibata, K., & Fang, C. 2002, ApJ, 572, L99
Cohen, O., Attrill, G. D. R., Manchester, W. B., & Wills-Davey, M. J. 2009, ApJ, 705, 587
Delannée, C. 2000, ApJ, 545, 512
Delannée, C., & Aulanier, G. 1999, Sol. Phys., 190, 107
Delannée, C., Hochedez, J.-F., & Aulanier, G. 2007, A&A, 465, 603
Delannée, C., Török, T., Aulanier, G., & Hochedez, J.-F. 2008, Sol. Phys., 247, 123
Downs, C., Roussev, I. I., van der Holst, B., et al. 2011, ApJ, 728, 2
Fludra, A., Del Zanna, G., Alexander, D., & Bromage, B. J. I. 1999, J. Geophys. Res., 104, 9709
Gallagher, P. T., & Long, D. M. 2011, Space Sci. Rev., 158, 365
Gary, G. A. 2001, Sol. Phys., 203, 71
Gopalswamy, N., Lara, A., Kaiser, M. L., & Bougeret, J.-L. 2001, J. Geophys. Res., 106, 25261
Gopalswamy, N., Yashiro, S., Temmer, M., et al. 2009, ApJ, 691, L123
Grechnev, V. V., Afanasyev, A. N., Uralov, A. M., et al. 2011, Sol. Phys.
Howard, R. A., Moses, J. D., Vourlidas, A., et al. 2008, Space Sci. Rev., 136, 67
Hudson, H. S., Khan, J. I., Lemen, J. R., Nitta, N. V., & Uchida, Y. 2003, Sol. Phys., 212, 121
Kaiser, M. L., Kucera, T. A., Davila, J. M., et al. 2008, Space Sci. Rev., 136, 5
Kienreich, I. W., Temmer, M., & Veronig, A. M. 2009, ApJ, 703, L118
Liu, W., Nitta, N. V., Schrijver, C. J., Title, A. M., & Tarbell, T. D. 2010, ApJ, 723, L53
Long, D. M., Gallagher, P. T., McAteer, R. T. J., & Bloomfield, D. S. 2008, ApJ, 680, L81
Ma, S., Wills-Davey, M. J., Lin, J., et al. 2009, ApJ, 707, 503
Moses, D., Clette, F., Delaboudinière, J.-P., et al. 1997, Sol. Phys., 175, 571
Narukage, N., Hudson, H. S., Morimoto, T., et al. 2002, ApJ, 572, L109
Ofman, L., & Thompson, B. J. 2002, ApJ, 574, 440
Ontiveros, V., & Vourlidas, A. 2009, ApJ, 693, 267
Patsourakos, S., & Vourlidas, A. 2009, ApJ, 700, L182
Patsourakos, S., Vourlidas, A., Wang, Y., Stenborg, G., & Thernisien, A. 2009, Sol. Phys., 259, 49
Saito, K., Poland, A. I., & Munro, R. H. 1977, Sol. Phys., 55, 121
Schrijver, C. J., & Derosa, M. L. 2003, Sol. Phys., 212, 165
Sheeley, N. R., Jr., Wang, Y.-M., Hawley, S. H., et al. 1997, ApJ, 484, 472
Steinolfson, R. S., & Hundhausen, A. J. 1988, J. Geophys. Res., 93, 14269
Thompson, B. J., Gurman, J. B., Neupert, W. M., et al. 1999, ApJ, 517, 151
Thompson, B. J., & Myers, D. C. 2009, ApJS, 183, 225
Thompson, B. J., Plunkett, S. P., Gurman, J. B., et al. 1998, Geophys. Res. Lett., 25, 2465
Totten, T. L., Freeman, J. W., & Arya, S. 1995, J. Geophys. Res., 100, 13
Veronig, A. M., Muhr, N., Kienreich, I. W., Temmer, M., & Vršnak, B. 2010, ApJ, 716, L57
Veronig, A. M., Temmer, M., & Vršnak, B. 2008, ApJ, 681, L113
Vourlidas, A., Wu, S. T., Wang, A. H., Subramanian, P., & Howard, R. A. 2003, ApJ, 598, 1392
Vršnak, B., & Cliver, E. W. 2008, Sol. Phys., 253, 215
Vršnak, B., Magdalenić, J., Temmer, M., et al. 2005, ApJ, 625, L67
Wang, H., Shen, C., & Lin, J. 2009, ApJ, 700, 1716
Wang, Y.-M. 2000, ApJ, 543, L89
Warmuth, A. 2007, in Lecture Notes in Physics, Vol. 725, The High Energy Solar Corona: Waves, Eruptions, Particles, ed. K.-L. Klein & A. L. MacKinnon (Berlin: Springer), 107
Warmuth, A., Mann, G., & Aurass, H. 2005, ApJ, 626, L121
Warmuth, A., Vršnak, B., Magdalenić, J., Hanslmeier, A., & Otruba, W. 2004, A&A, 418, 1101
White, S. M., & Thompson, B. J. 2005, ApJ, 620, L63
Wills-Davey, M. J., & Attrill, G. D. R. 2009, Space Sci. Rev., 149, 325
Wills-Davey, M. J., DeForest, C. E., & Stenflo, J. O. 2007, ApJ, 664, 556
Wills-Davey, M. J., & Thompson, B. J. 1999, Sol. Phys., 190, 467
Wu, S. T., Guo, W. P., Michels, D. J., & Burlaga, L. F. 1999, J. Geophys. Res., 104, 14789
Wu, S. T., Li, B., Wang, S., & Zheng, H. N. 2005, J. Geophys. Res., 110, A11102
Wu, S. T., Zheng, H., Wang, S., et al. 2001, J. Geophys. Res., 106, 25089
Yang, H. Q., & Chen, P. F. 2010, Sol. Phys., 226, 59
Zhao, X. H., Feng, X. S., Xiang, C. Q., et al. 2010, ApJ, 714, 1133
Zhukov, A. N., & Auchère, F. 2004, A&A, 427, 705